

TINQ: Temporal Inconsistency Guided Blind Video Quality Assessment

Yixiao Li^{1*}, Xiaoyuan Yang^{1†}, Weide Liu², Xin Jin³, Xu Jia⁴,
Yukun Lai⁵, Hantao Liu⁵, Paul L. Rosin⁵, Wei Zhou^{5†}

¹Beihang University, China ²Harvard University, USA ³Eastern Institute of Technology, China

⁴Dalian University of Technology, China ⁵Cardiff University, UK

Email: 18335310648@163.com xiaoyuanyang@vip.163.com zhouw26@cardiff.ac.uk

Abstract

Blind video quality assessment (BVQA) has been actively researched for user-generated content (UGC) videos. Recently, super-resolution (SR) techniques have been widely applied in UGC. Therefore, an effective BVQA method for both UGC and SR scenarios is essential. Temporal inconsistency, referring to irregularities between consecutive frames, is relevant to video quality. Current BVQA approaches typically model temporal relationships in UGC videos using statistics of motion information, but inconsistencies remain unexplored. Additionally, different from temporal inconsistency in UGC videos, such inconsistency in SR videos is amplified due to upscaling algorithms. In this paper, we introduce the **Temporal Inconsistency Guided Blind Video Quality Assessment (TINQ)** metric, demonstrating that exploring temporal inconsistency is crucial for effective BVQA. Since temporal inconsistencies vary between UGC and SR videos, they are calculated in different ways. Based on this, a spatial module highlights inconsistent areas across consecutive frames at coarse and fine granularities. In addition, a temporal module aggregates features over time in two stages. The first stage employs a visual memory capacity block to adaptively segment the time dimension based on estimated complexity, while the second stage focuses on selecting key features. The stages work together through Consistency-aware Fusion Units to regress cross-time-scale video quality. Extensive experiments on UGC and SR video quality datasets show that our method outperforms existing state-of-the-art BVQA methods. Code is available at <https://github.com/Lighting-YXLI/TINQ>.

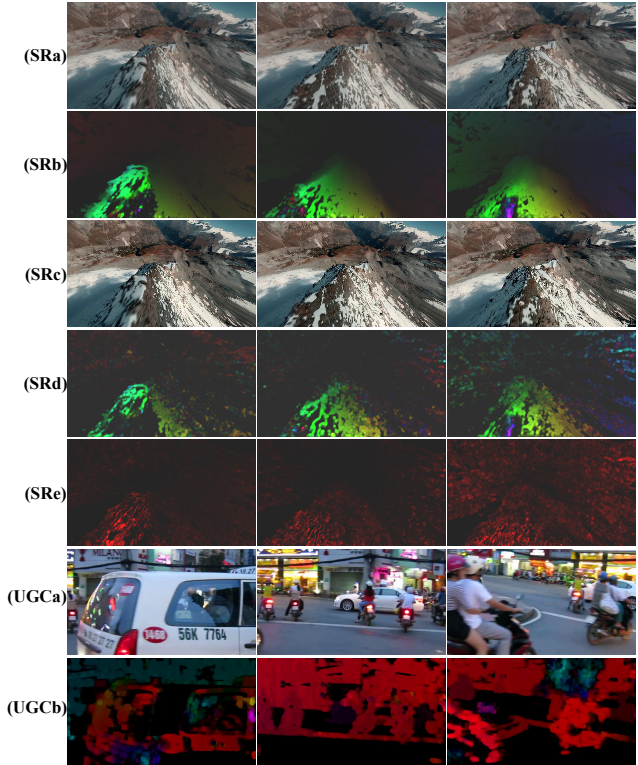


Figure 1. **Temporal inconsistency is what BVQA needs!** Rows (SRa)–(SRe) show consecutive frames from VSR-QAD [48], and rows (UGCa) and (UGCb) are from KoNViD-1K [17]. (SRa) is a reference video, (SRb) is the optical flow of (SRa), (SRc) is the SR video, (SRd) is the optical flow of (SRc), and (SRe) is the **temporal inconsistency video** for (SRc), derived as the difference between (SRb) and (SRd). (UGCa) is a UGC video, and (UGCb) is its **temporal inconsistency video**, represented by the optical flow of (UGCa). The methods for computing temporal inconsistency differ for SR and UGC videos, the reasons are analyzed in Fig. 2.

1. Introduction

The rapid advancements in video processing and transmission technologies have led to an exponential increase in

*This work was done when Yixiao Li was an academic visitor at Cardiff University.

†Corresponding author.

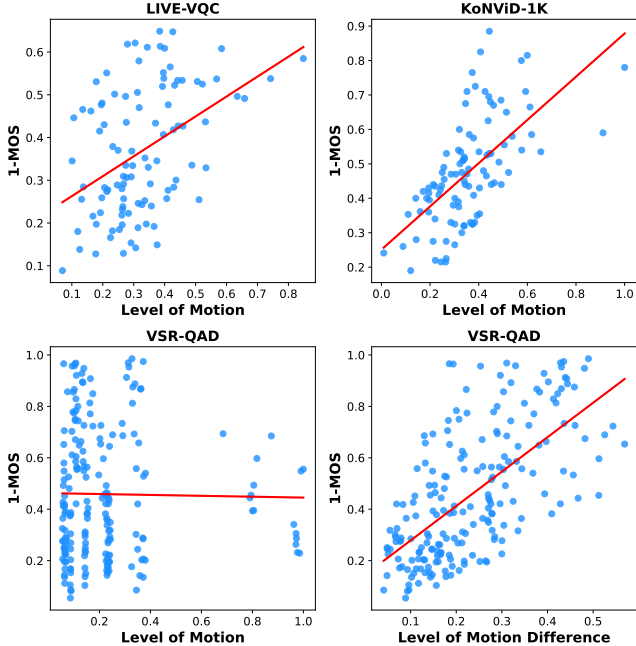


Figure 2. To compute temporal inconsistency for UGC and SR videos, we randomly sampled UGC videos from KoNViD-1K [17] and LIVE-VQC [33], and SR videos from VSR-QAD [48]. We calculate motion levels using the video complexity metric in Section 3.1 and analyzed their correlation with video quality (1-MOS). In UGC datasets, motion level obviously correlates with quality. But this correlation does not hold for the SR dataset. SR videos, with amplified temporal inconsistencies, have this information masked by the richer motion from reference videos. Thus, we define temporal inconsistency for SR videos as the motion (optical flow) difference between an SR video and its reference, which shows a strong correlation with quality (bottom right image). The formula is in Eq. 17.

diverse video content, significantly influencing daily life. To evaluate the perceived quality of these videos, several user-generated content (UGC) video quality assessment datasets [17, 33, 40] have been developed, driving the evolution of video quality assessment (VQA) methods. Recently, with the demand for higher resolution content, super-resolution (SR) techniques have been widely applied in the UGC scenario [20], but developing a VQA metric suitable for both UGC and SR scenarios is still a challenge.

Given the impracticality of acquiring perfect reference videos for real-world content, blind video quality assessment (BVQA) methods [1–3, 5, 12, 19, 21, 22, 27, 34, 36, 37, 39, 42, 48, 51] have gained significant attention. Temporal inconsistency, referring to irregularities or discrepancies in dynamic scenes (including motion, transitions, visual changes, etc.) over time that deviate from the expected smooth flow of visual information between consecutive frames, is a key aspect in BVQA. Latest BVQA methods typically model temporal relationships through vari-

ous techniques, such as frame differences [1, 51], optical flow [51], temporal slicing [12, 48], natural scene statistics [22, 27], and 3D CNNs [21, 39] applied to distorted videos. However, none of the above methods try to design quality assessment metrics from the perspective of temporal inconsistency.

Moreover, the growth of SR technologies [4, 18] has made temporal inconsistencies amplified due to the up-sampling processes. The recently proposed VSR-QAD dataset [48] was specifically designed to assess SR video quality, but the effectiveness of current BVQA techniques for such videos remains unstable [48].

Since temporal inconsistency is a common attribute in both UGC and SR videos, proposing a BVQA method guided by temporal inconsistency can be suitable for both scenarios. Considering that temporal inconsistency in SR videos is different from that in UGC videos, we compute the inconsistency information specifically for UGC and SR scenarios, respectively. Then we propose the **Temporal Inconsistency Guided Blind Video Quality Assessment (TINQ)** metric, which integrates temporal inconsistency as guidance in both spatial and temporal dimensions during model training.

For the SR scenario, we propose to derive temporal inconsistency by calculating the difference between the optical flows of SR and the corresponding reference videos. These videos effectively display motion artifacts in distorted videos relative to their references (as shown in Figure 1). For the UGC scenario, the reference is unavailable, but such temporal inconsistency can be reasonably measured by optical flow, following the analysis in Fig. 2, which provides empirical support for using temporal inconsistency information to guide quality prediction for both UGC and SR videos.

As the proposed TINQ belongs to BVQA, during training, we highlight temporally inconsistent areas of distorted videos by weighting with the extracted temporal inconsistency information. During testing, the distorted video is directly input for quality prediction. We extract spatial features at both coarse and fine levels. For coarse grain, we design a deformable window super attention (DW-SA) Transformer to **capture inconsistencies in major scene changes or fast movements**, leveraging the global receptive field of Transformers [23]. For fine grain, CNNs are employed to **detect subtle inconsistencies in slower scene transitions or minor motions**, drawing on their effectiveness in capturing local details [15]. The final spatial features are obtained by concatenating both coarse and fine features.

We then propose a two-stage temporal aggregation guided by inconsistency. Specifically, the first stage is based on the visual working memory (VWM) mechanism. Current BVQA methods’ exploration of the VWM is limited [2, 22]. Although these methods address the VWM

mechanism, they overlook the critical capacity limitation that occurs in VWM [7,9,29,43]. Our work designs a visual memory capacity block, dynamically aggregating temporal features based on the level of temporal inconsistency. In the second stage, the time dimension is aggregated by key feature selection. In both stages, a Consistency-aware Fusion Unit is introduced to model temporal relationships, finally leading to a cross-multi-time scale quality prediction.

The contributions of this paper are as follows:

1. We propose the Temporal Inconsistency Guided Blind Video Quality Assessment (TINQ) method, leveraging temporal inconsistency to guide quality assessment and validate both its rationale and effectiveness. The rule of temporal inconsistency computation differs for UGC and SR scenarios.
2. We introduce the Inconsistency Highlighted Spatial Module, emphasizing pixel-level temporally inconsistent areas. This module incorporates a DW-SA Transformer for coarse-grained spatial feature extraction, along with a CNN to provide fine-grained details.
3. We present the Inconsistency Guided Temporal Module, featuring a visual memory capacity block that dynamically allocates memory threshold for temporal feature segmentation based on inconsistency levels. Additionally, Consistency-aware Fusion Units are proposed for temporal aggregation, enabling a cross-time-scale prediction of video quality.
4. Experimental results demonstrate the superiority of our BVQA model over existing methods on several video quality datasets, covering both UGC [17,33] and SR [48].

2. Related Work

2.1. Temporal Relationship Modeling in BVQA

Several publicly available UGC VQA datasets [17,33] have provided a solid foundation for evaluating real-world video distortions. Contemporary BVQA methods have actively explored feature extraction strategies for modeling temporal relationships. These approaches can be broadly categorized into five types: frame difference [1,51], optical flow [51], spatio-temporal slicing [12,48], 3D-CNNs [21,39], and multi-level based methods [19,27]. However, many BVQA models rely heavily on handcrafted features to capture temporal features. Specifically, BLIINDS [27] designs features to assess motion coherence and global motion (egomotion). TLVQM [19] employs low-level and high-level frame complexity and uses the standard deviation of temporal features. Recently, there has been a shift towards purely learning-based methods, such as VSFA [22], STI-VQA [51], and Wild-BVQA [21], which utilize various pre-trained networks as fixed feature extractors and independently train regression modules.

While existing BVQA methods are developed for the UGC scenario, they have overlooked the role of tempo-

ral inconsistencies in assessing videos. Additionally, these approaches are unstable in the SR scenario which contains amplified temporal inconsistencies. The VSR-QAD dataset [48] is currently the only resource specifically designed for this purpose. However, none of the existing works have attempted to design models suitable for both UGC and SR datasets.

2.2. Visual Working Memory Mechanism

Recent research in psychology has underscored the importance of the visual working memory (VWM) mechanism in shaping visual perception [26,32]. Despite this, its role in VQA tasks remains relatively unexplored. Neuroscientific studies have shown that memory performance improves with the increased salience of visual objects [28]. In VM-VQA [2], this concept is utilized by generating saliency maps based on Complete Local Binary Patterns from residual frames, and then modeling visual memory using statistical data from these maps. VSFA [22] introduces a differentiable temporal pooling model to account for time-lag effects.

A key characteristic of visual working memory is its capacity limitation — which is involved in the storing and processing of visual information [32,43]. The storage capacity is usually limited to around 3 to 7 visual objects [7,43], and memory accuracy decreases as object complexity increases [9,29]. Research has further revealed that VWM not only stores information but also dynamically manages it by prioritizing the storage of critical features, thereby enhancing task performance and adaptability [11,14]. The memory capacity has not yet been leveraged for VQA tasks, and here we propose the temporal module based on a visual memory capacity mechanism to better capture visual perception.

3. Proposed Method

In this work, we propose a **Temporal Inconsistency Guided Blind Video Quality Assessment** method, as illustrated in Figure 3. Note that the representations of temporal inconsistency for UGC and SR scenarios are slightly different, the reason is analyzed in Figure 2.

3.1. Inconsistency Highlighted Spatial Module

In this subsection, we introduce the inconsistency guidance for spatial dimension.

In the **training process**, we first obtain the temporally inconsistent areas of distorted videos. For the SR scenario, take a pair of SR video and the corresponding reference V_D , $V_R \in \mathbb{R}^{F \times W \times H \times 3}$ as inputs, where F is the total number of frames, and $W, H, 3$ denote the width, height, and number of channels of each frame, respectively. For the UGC scenario, take the distorted video V_D as input. The temporal

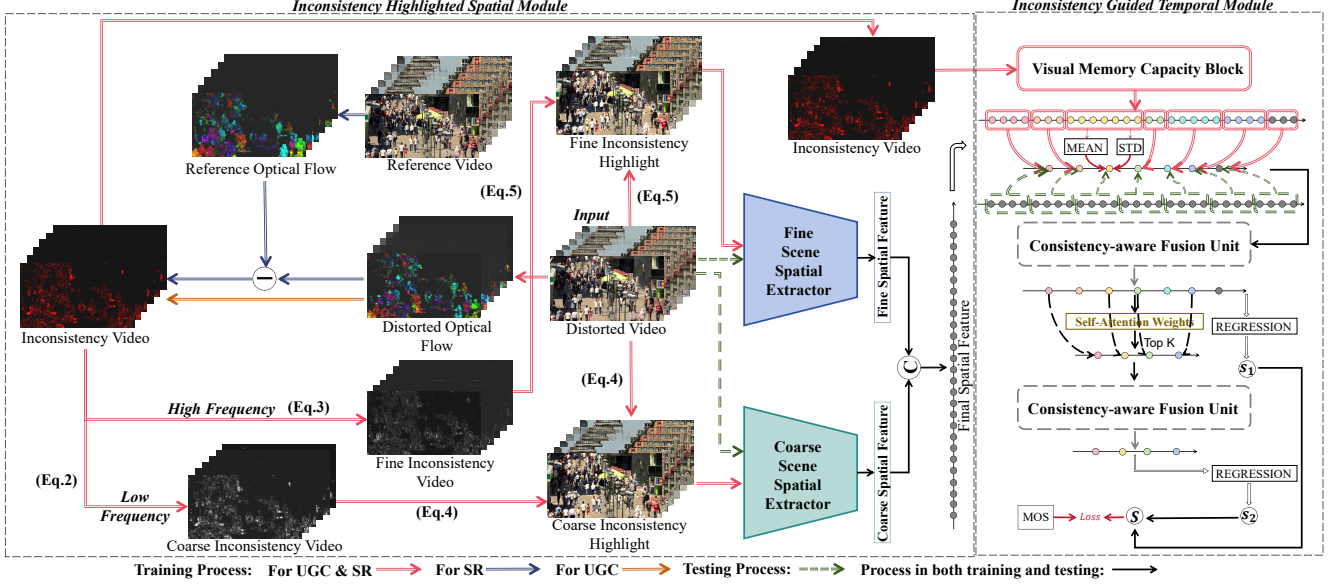


Figure 3. The proposed TINQ framework. The processes for SR and UGC scenarios differ slightly in how to compute the Inconsistency Video. The spatial module calculates temporal inconsistency at coarse and fine granularities, using pixel-level weighting to emphasize inconsistent regions in distorted videos, guiding the network’s learning. The temporal module estimates the level of temporal inconsistency and constructs a memory capacity block. During temporal aggregation, it regresses quality scores S_1, S_2 at different temporal scales and outputs the final quality score S .

inconsistency information V_I is captured as follows:

$$V_I = \begin{cases} \|(OF(V_R) - OF(V_D))\|_2, V_D \in \text{SR video}, \\ \|(OF(V_D))\|_2, V_D \in \text{UGC video}, \end{cases} \quad (1)$$

where $OF(\cdot)$ refers to optical flow computation. $\|(\cdot)\|_2$ is 2-norm.

Then, we divide the temporal inconsistency information into coarse and fine granularities. The coarse-grain aims to capture temporal inconsistencies in rapidly changing regions, such as significant scene changes or fast-moving areas. We apply the Gaussian low-pass filter to video V_I in the frequency domain:

$$V_I^C = \mathcal{F}^{-1}(H_L \cdot \mathcal{F}(V_I)), \quad (2)$$

where \mathcal{F} and \mathcal{F}^{-1} denote the Fourier transform and inverse Fourier transform, respectively. H_L is the Gaussian low-pass filter. The cutoff frequency of the Gaussian filter is empirically set to 5% of the long dimension of the frame [13]. Similarly, the fine-grain aims to capture subtle temporal inconsistencies, such as those occurring in slow scene transitions or minor motions. This is achieved by applying the Gaussian high-pass filter to video V_I in the frequency domain:

$$V_I^F = \mathcal{F}^{-1}(H_H \cdot \mathcal{F}(V_I)), \quad (3)$$

$$H_H = 1 - H_L.$$

Then, V_I^C and V_I^F are normalized and weighted with distorted video, so that the temporal inconsistent areas can be highlighted:

$$\hat{V}_D^C = Norm(V_I^C) \times V_D + V_D, \quad (4)$$

$$\hat{V}_D^F = Norm(V_I^F) \times V_D + V_D, \quad (5)$$

where \hat{V}_D^C and \hat{V}_D^L are the coarse inconsistency highlighted video and fine inconsistency highlighted video, both clipped to $[0, 255]$, $Norm(\cdot)$ refers to normalization to be within $[0, 1]$.

For the coarse scene spatial extractor, we propose a Transformer-based model, which has proven highly effective in capturing long-range dependencies [23]. Specifically, we propose the Deformable-window Super-Attention (DW-SA) Transformer block. Considering that deformable technology is empirically designed in the later stages of the network [8, 52], the proposed DW-SA-T block replaces the Swin-T blocks in the third stage rather than the early stages. As shown in Figure 4, the DW-SA-T block introduces adaptive offset vectors for each window, inspired by deformable convolutions [8, 52] widely applied in dense prediction tasks. Before computing self-attention, each window is up-sampled using sub-pixel convolution [31] and then shifted. Since sub-pixel convolution was designed for image super-resolution, the DW-SA-T block benefits for paying attention to both SR-based and natural temporal inconsistency information. The consecutive DW-SA Transformer blocks are

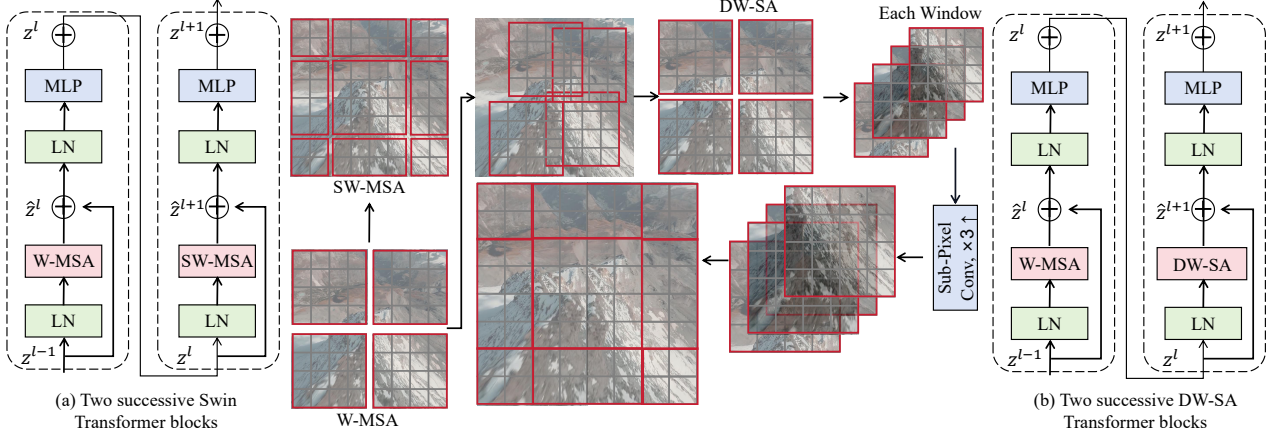


Figure 4. The details of proposed Deformable-window Super Attention (DW-SA) Transformer block. The proposed DW-SA Transformer block adapts window sampling locations, up-samples features within each window, and then shifts them. W-MSA and SW-MSA refer to the standard and shifted multi-head self-attention blocks from Swin-T [23].

computed as:

$$\begin{aligned}
 \hat{z}^l &= \text{W-MSA} \left(\text{LN} \left(z^{l-1} \right) \right) + z^{l-1} \\
 z^l &= \text{MLP} \left(\text{LN} \left(\hat{z}^l \right) \right) + \hat{z}^l \\
 \hat{z}^{l+1} &= \text{DW-SA} \left(\text{LN} \left(z^l \right) \right) + z^l \\
 z^{l+1} &= \text{MLP} \left(\text{LN} \left(\hat{z}^{l+1} \right) \right) + \hat{z}^{l+1},
 \end{aligned} \tag{6}$$

where \hat{z}^l and z^l denote the output features of the W-MSA and DW-SA modules and the MLP module for block l , respectively; W-MSA and LN denote window based multi-head self-attention and layer norm of Swin-T, respectively.

For \hat{V}_D^F , we utilize ResNet [15] to capture spatial features. Both coarse and fine scene spatial extractors are pre-trained on ImageNet-1k [10]. Given input $\hat{V}_D^C, \hat{V}_D^F \in \mathbb{R}^{F \times W \times H \times 3}$, the coarse scene extractor first resizes \hat{V}_D^C from $F \times W \times H \times 3$ to $F \times 224 \times 224 \times 3$, while the fine scene extractor processes \hat{V}_D^F directly. The details of feature extraction are shown in Table 1.

Table 1. The details of spatial feature extraction. μ, σ are the mean and standard deviation calculation, respectively.

Feature Shapes	Coarse Scene	Fine Scene
Input features	$F \times 224 \times 224 \times 3$	$F \times W \times H \times 3$
Stem	$F \times \frac{224}{4} \times \frac{224}{4} \times 48$	$F \times \frac{W}{4} \times \frac{H}{4} \times 64$
Stage 1	$F \times \frac{224}{4} \times \frac{224}{4} \times 96$	$F \times \frac{W}{8} \times \frac{H}{8} \times 256$
Stage 2	$F \times \frac{224}{8} \times \frac{224}{8} \times 192$	$F \times \frac{W}{16} \times \frac{H}{16} \times 812$
Stage 3	$F \times \frac{224}{16} \times \frac{224}{16} \times 384$	$F \times \frac{W}{32} \times \frac{H}{32} \times 1024$
Stage 4	$F \times \frac{224}{32} \times \frac{224}{32} \times 768$	$F \times \frac{W}{64} \times \frac{H}{64} \times 2048$
$[\mu, \sigma]$	$[F \times 768, F \times 768]$	$[F \times 2048, F \times 2048]$

The final spatial features $F_S \in \mathbb{R}^{F \times 5632}$ are as follows:

$$\begin{aligned}
 F_S^C &= \text{Extractor}_C(\hat{V}_D^C), \\
 F_S^F &= \text{Extractor}_F(\hat{V}_D^F), \\
 F_S &= \text{Concatenate}(V_S^C, V_S^F),
 \end{aligned} \tag{7}$$

where the detailed network design for the coarse and fine feature extractors Extractor_C and Extractor_F is presented in the supplementary material.

In the **testing process**, both spatial extractors take V_D as input, so that reference information is removed.

3.2. Inconsistency Guided Temporal Module

In this subsection, we propose a two-stage temporal aggregation integrating cross-time-scale relationships. One of the key factors in temporal aggregation is determining the appropriate amount of information that each time segment should load. Recent psychological research on the visual working memory mechanism [7, 9, 11, 14, 29, 43] has yielded exciting findings regarding memory capacity, showing that human visual working memory has a capacity limit when temporarily storing and processing visual information. Moreover, this capacity is dynamically allocated based on the complexity of the scene changes.

Therefore, in the first stage of time aggregation, we design a visual memory capacity block. Since the temporal inconsistency video V_I reflects the level of scene changes in the distorted video relative to the reference, we assess the complexity of V_I to determine the memory threshold (i.e., capacity). This block is applied during **training** and removed during **testing**, as shown in Figure 3.

We separately compute the spatial complexity of each frame and then determine the complexity of the video. As V_I contains optical flow information, the magnitude of each

frame and directional consistency are taken into account:

$$C_I^{ij} = \alpha \times (\sigma(M(V_I^{ij}))) + (1 - \alpha) \times (\sigma(D(V_I^{ij}))), \quad (8)$$

$$i = 1, \dots, N; j = 1, \dots, F.$$

where N and F are the number of videos and frame count for each video, respectively. $M(\cdot)$ refers to magnitude computation, and $D(\cdot)$ calculates the direction of the difference between adjacent frames, generating a histogram of the directions, and then the standard deviation σ of the histogram represents the directional consistency. α is a hyper-parameter. Then, the complexity of video V_I is calculated as follows:

$$C_I^i = \mu(\{C_I^{ij} \mid j = 1, \dots, F\}) + \sigma(\{C_I^{ij} \mid j = 1, \dots, F\}), i = 1, \dots, N. \quad (9)$$

where μ and σ refer to mean and standard deviation, respectively. $C_I = \{C_I^i\}$ is then normalized to $[0, 1]$. Moreover, the rationale of the above calculation is detailed in the supplementary materials. Then the input features F_S can be segmented by the following visual memory capacity block, as shown in Algorithm 1, which follows two principles:

1. Dynamic allocation of memory threshold in a range.
2. When the level of time inconsistency increases, the memory threshold decreases.

Principle 1 aligns with psychological research [7, 11, 14, 43], which suggests that memory capacity in humans is approximately 3-7 objects and dynamically adjusted according to scene complexity. Principle 2 is supported by psychological studies [9, 29], which shows that increased scene complexity negatively impacts memory performance.

Then, we model the temporal relationships of the first-stage features F_A , regressing them to obtain the first-stage quality score S_1 . Recognizing that Long Short-Term Memory (LSTM) models [6, 16] are insufficient for capturing complex temporal dependencies, we propose a Consistency-aware Fusion Unit $-F'_A$, described as follows:

First, we calculate the sparse adjacency matrix of input features $Adj(F_A)$. Each node feature h_i of F_A is then transformed using a learnable weight matrix W to increase the representational capacity:

$$W_h(i) = Wh_i, \quad (10)$$

where W is the weight matrix shared across all nodes. Then, the attention coefficients e_{ij} between node i and its neighbor j are computed by concatenating the transformed features of the two nodes, followed by applying a shared attention mechanism:

$$e_{ij} = \text{LeakyReLU}(a^T [W_h(i) \| W_h(j)]), \quad (11)$$

where a is the learnable attention vector and $\|$ denotes concatenation. Then filter $e = \{e_{ij}\}$ based on the positive elements of $Adj(F_A)$:

$$e_{ij} = \begin{cases} e_{ij} & Adj(F_A)_{ij} > 0 \\ 0 & Adj(F_A)_{ij} \leq 0 \end{cases}$$

Algorithm 1 Visual Memory Capacity Block

Input: Final spatial features $F_S^i \in \mathbb{R}^{F \times 5632}$, and temporal inconsistency levels $C_I^{ij} \in \mathbb{R}^{F \times F}$ and $C_I^i \in \mathbb{R}^1$, where $i = 1, \dots, N; j = 1, \dots, F$. N is the number of input videos, F is frame count.

Output: Aggregated Features $F_A^i, i = 1, \dots, N$.

- 1: Compute the adaptive memory threshold of distorted video V_D^i as:

$$T_D^i = \tau - \eta \times \frac{C_I^i - \text{MIN}(\{C_I^i\})}{\text{MAX}(\{C_I^i\}) - \text{MIN}(\{C_I^i\})}.$$
 - 2: # The final settings of τ is 5 and η is 1.
 - 3: Adaptively segment input features F_S^i :
 - Set of segments: $S = \emptyset$;
 - Current segment: $S_C = \emptyset$;
 - 4: **for** $j \in [1, F]$ **do**
 - 5: Current complexity: $C_C + = C_I^{ij}$
 - 6: Add F_S^{ij} to S_C : $S_C.append(F_S^{ij})$
 - 7: **if** $C_C \geq T_D^i$ **then**
 - 8: $S.append(S_C)$
 - 9: $S_C = \emptyset$
 - 10: $C_C = 0$
 - 11: **end if**
 - 12: **end for**
 - 13: **for** $k \in N_S$ **do**
 - 14: $F_A^{ik} = \text{Concatenate}(\text{MEAN}(S_k) + \text{STD}(S_k))$
 - 15: **end for**
 - 16: #Where N_S is the number of segments in S .
-

The attention coefficients are normalized using the softmax function:

$$\alpha_{ij} = \frac{\exp(e_{ij})}{\sum_{k \in \mathcal{N}(i)} \exp(e_{ik})}, \quad (12)$$

where $\mathcal{N}(i)$ represents the neighbors of node i . Finally, the new feature h'_i of node i is computed by aggregating its neighbors' features weighted by the attention coefficients:

$$h'_i = \phi \left(\sum_{j \in \mathcal{N}(i)} \alpha_{ij} W_h(j) \right), \quad (13)$$

where ϕ is a non-linear activation function (e.g., ELU or ReLU). And the features after time modeling are obtained by the Gated Recurrent Unit (GRU) [6]:

$$F'_A = \text{GRU}(\{h'_i\}). \quad (14)$$

F'_A is then used for the second-stage time aggregation. In this stage, we filter key features to model temporal relationships. Specifically, self-attention is computed on the output F'_A from the first stage, and the top K features with the highest attention scores are selected as key features:

$$S = SA(F'_A) \quad (15)$$

$$F''_A = F'_A[\text{Top}_K(S)],$$

where SA represents self-attention. S is the attention weight. The F''_A is then processed by another Consistency-aware Fusion Unit, which regresses the second-stage quality score S_2 . The final quality prediction is computed as:

$$S = \gamma \times S_1 + (1 - \gamma) \times S_2, \quad (16)$$

where γ is a hyper-parameter. All the hyper-parameters are determined through ablation studies, as detailed in supplementary material.

4. Experiments

In this section, we first describe the experimental setups. We then present the experimental results on one SR dataset and two UGC datasets, with computational analysis displayed in supplementary material. Last, we conduct a set of validity experiments to complete our model analysis.

4.1. Experimental Setups

Benchmark Datasets. We validate TINQ on both super-resolution and user-generated content distortions. For super-resolution, we employ VSR-QAD [48], the only public SR VQA dataset, containing 120 reference videos down-sampled by factors of $\times 2$, $\times 4$, and $\times 8$, and upscaled by 10 SR algorithms, resulting in 2,260 videos after outlier filtering. For real world distortions, we use KoNViD-1K [17] (1,200 UGC videos) and LIVE-VQC [33] (585 UGC videos with over 205,000 opinion scores).

Competing Methods. For the SR scenario, we evaluate full-reference (FR) methods (PSNR, SSIM [38], VIF [30], VMAF [25], SRIF [50]), reduced-reference (RR) methods (SpEED-QA [1], IGTS [35], DISQ [44], DR-IQA [45], STF [47], VSR-QAD), and no-reference (NR) methods (DeepSRQ [49], VIDEVAL [37], VSFA [22], GSTVQA [5], STI-VQA [51], 2Bi-VQA [36], MBVQA [39]). Among them, SRIF, IGTS, DISQ, STF, DeepSRQ are SR IQA methods, and VSR-QAD is the first SR VQA method. For natural distortions, we use VSFA, TLVQM [19], VIDEVAL, VISION [24], SimpleVQA [34], VIQE [46], 2Bi-VQA, STFR, and MBVQA.

Performance Criteria. We evaluate performance using Spearman rank-order correlation coefficient (SRCC), Kendall rank-order correlation coefficient (KRCC), Pearson linear correlation coefficient (PLCC), and root mean square error (RMSE). For VSR-QAD, we follow its protocols: randomly splitting videos into 70% training, 10% validation, and 20% testing. VSFA, 2Bi-VQA, and MBVQA are re-trained, with other results cited from VSR-QAD. For UGC datasets, we split them into 60% training, 20% validation, and 20% testing, repeating the process 10 times and reporting median results.

Implementation Details. Models were trained for 100 epochs on an NVIDIA RTX 3080 Ti with PyTorch 1.7.1. Temporal inconsistency videos guided both spatial and temporal modules during training, and were removed during testing. The Adam optimizer was used with an initial learning rate of 10^{-5} , decaying by 0.8 every 10 epochs. Batch size was 16, with no weight decay. The loss combined SRCC and MSE to leverage both ranking and regression.

Table 2. Performance comparison of our methods against competing IQA/VQA methods on the first large-scale SR VQA dataset (VSR-QAD). The best performance is highlighted. The original MBVQA is pretrained on large-scale dataset LSVQ [41], so we trained MBVQA* on VSR-QAD without pretraining for fairness.

Methods		SRCC \uparrow	PLCC \uparrow	KRCC \uparrow	RMSE \downarrow
FR	PSNR	0.6446	0.6551	0.4677	0.1995
	SSIM [38]	0.6956	0.7098	0.5252	0.1885
	VIF [30]	0.7459	0.7531	0.5785	0.1647
	VMAF [25]	0.7096	0.7229	0.5386	0.1839
	SRIF [50]	0.7431	0.7505	0.5756	0.1688
RR	SpEED-QA [1]	0.5041	0.5162	0.3068	0.2447
	IGTS [35]	0.5334	0.5498	0.3367	0.2336
	DISQ [44]	0.6421	0.6498	0.4653	0.2024
	DR-IQA [45]	0.7074	0.7163	0.5369	0.1843
	STF [47]	0.7629	0.7691	0.5942	0.1629
	VSR-QAD [48]	0.8601	0.8681	0.6872	0.1253
NR	DeepSRQ [49]	0.6665	0.6556	0.4741	0.1949
	VIDEVAL [37]	0.7443	0.7492	0.5769	0.1671
	VSFA [22]	0.8081	0.8123	0.6301	0.1524
	GSTVQA [5]	0.8278	0.8251	0.6453	0.1473
	STI-VQA [51]	0.8228	0.8293	0.6479	0.1469
	2Bi-VQA [36]	0.7766	0.8099	0.5854	0.6649
	MBVQA* [39]	0.8924	0.9008	0.7167	0.1057
	TINQ	0.9386	0.9417	0.7940	0.0827

4.2. Results on VSR-QAD dataset

Table 2 highlights the performance of various IQA/VQA methods on the VSR-QAD dataset. Comparing TINQ with other methods in the NR category, MBVQA is the closest competitor but still falls short in all key metrics, particularly KRCC and RMSE. This highlights TINQ’s stronger ability to maintain rank correlation and minimize prediction errors. While models like GSVTQA and STI-VQA perform well, TINQ surpasses them. In the RR and FR categories, TINQ also outperforms others. This showcases TINQ’s capacity to make accurate video quality predictions without relying on reference data, providing a major advantage in practical scenarios where reference might not be available.

4.3. Results on UGC datasets

Table 3 shows that TINQ consistently outperforms other VQA methods on both the KoNViD-1K and LIVE-VQC datasets. On KoNViD-1K, TINQ achieves the highest PLCC (0.844) and SRCC (0.842), matches the models like MBVQA, 2Bi-VQA, and STFR. Similarly, on LIVE-VQC, TINQ leads with a PLCC of 0.838 and SRCC of 0.808, indicating its robust capability in assessing UGC video quality.

4.4. Validity on Cross datasets

As shown in Table 4, cross-dataset testing reveals a critical generalization comparison between our TINQ and two competing models, 2Bi-VQA and MBVQA. When trained on the VSR-QAD dataset and tested on the KoNViD-1K and LIVE-VQC datasets, TINQ outperforms both 2Bi-VQA and MBVQA. Furthermore, when tested on the VSR-QAD dataset, TINQ again shows strong performance, demonstrating its superior generalizability across datasets.

Table 3. Performance comparison of our methods against competing UGC VQA methods on two large-scale UGC datasets. Note that the results of MBVQA were achieved after pretraining on the large-scale LSVQ [41] dataset, then fine-tuning on KoNViD-1K and LIVE-VQC. In contrast, other competitive methods were not pretrained on LSVQ. Therefore, we retrained MBVQA* without pretraining to ensure consistency in comparison. The best performance is highlighted.

Datasets	Metrics	VSFA	TLVQM	VIDEVAL	VISION	SimpleVQA	VIQE	2Bi-VQA	STFR	MBVQA*	MBVQA	TINQ
KoNViD-1K	PLCC↑	0.755	0.764	0.772	0.632	0.798	0.638	0.835	0.826	0.821	0.905	0.844
	SRCC↑	0.788	0.760	0.774	0.598	0.792	0.628	0.815	0.822	0.829	0.901	0.842
LIVE-VQC	PLCC↑	0.663	0.432	0.752	0.689	0.775	0.694	0.832	0.805	0.831	0.880	0.838
	SRCC↑	0.640	0.450	0.751	0.676	0.740	0.660	0.761	0.801	0.749	0.860	0.808

Table 4. Cross-dataset testing of our method against two competing methods. The best performance is highlighted. The MBVQA* is not pretrained on LSVQ [41].

Methods		TINQ		2Bi-VQA		MBVQA*	
Train	Test	SRCC↑	PLCC↑	SRCC↑	PLCC↑	SRCC↑	PLCC↑
VSR-QAD	KoNViD-1K	0.7007	0.6594	0.6776	0.6653	0.6107	0.6006
VSR-QAD	LIVE-VQC	0.6303	0.6873	0.6146	0.6717	0.6271	0.6379
KoNViD-1K	LIVE-VQC	0.8041	0.8127	0.7677	0.8398	0.6361	0.6492
KoNViD-1K	VSR-QAD	0.5654	0.5730	0.4043	0.3913	0.5259	0.5444
LIVE-VQC	KoNViD-1K	0.7334	0.7523	0.7764	0.7590	0.6741	0.6599
LIVE-VQC	VSR-QAD	0.4060	0.3792	0.3200	0.3220	0.3451	0.3712

Table 5. Fused-dataset validation of our method against two competing methods. The best performance is highlighted. The MBVQA* is not pretrained on LSVQ [41].

Datasets	VSR-QAD & LIVE-VQC				VSR-QAD & LIVE-VQC			
	SRCC↑	PLCC↑	KROCC↑	RMSE↓	SRCC↑	PLCC↑	KROCC↑	RMSE↓
2Bi-VQA	0.5336	0.4454	0.3809	1.9388	0.5107	0.4134	0.3579	2.0220
MBVQA*	0.8975	0.9267	0.7327	0.0870	0.8712	0.8852	0.6952	0.0982
TINQ	0.9279	0.9378	0.7750	0.0859	0.9494	0.9438	0.8087	0.0802

4.5. Validity on Fused datasets

To further validate the applicability of TINQ for both natural and super-resolution distortions, we merged the VSR-QAD and UGC datasets for model training. Table 5 presents a comparison of the TINQ with the other state-of-the-art BVQA methods on the fused dataset. Both SRCC and PLCC values indicate that TINQ achieves the highest performance across all aspects, demonstrating its robustness in video quality assessment. In contrast, while MBVQA performs well, its scores fall short of TINQ’s precision. The 2Bi-VQA exhibits significantly lower performance, highlighting its limitations in effectively assessing video quality across different distortion scenarios compared to TINQ and MBVQA.

4.6. Validity on Components of TINQ

The ablation study on the TINQ highlights the importance of each of its key components, as shown in Table 6. **w/o DW-SA** refers to TINQ without the proposed DW-SA Transformer blocks, using Swin-T blocks instead. **w/o Inconsistency Highlight** refers to using distorted videos as input without highlighting by temporal inconsistency videos in the spatial module. **w/o Memory Capacity** refers to removing the visual memory capacity block in the temporal module. **w/o Inconsistency Guidance** refers to not using

Table 6. Ablation experiments on each component of the proposed TINQ. The best performance is highlighted.

Methods	SRCC↑	PLCC↑	KRCC↑	RMSE↓
w/o DW-SA	0.8846	0.9131	0.7146	0.0967
w/o Inconsistency Highlight	0.8908	0.9088	0.7158	0.1164
w/o Memory Capacity	0.9081	0.921	0.7356	0.0945
w/o Inconsistency Guidance	0.8784	0.9010	0.7072	0.1074
Coarse Spatial Branch	0.7890	0.8464	0.6091	0.1305
Fine Spatial Branch	0.9263	0.9271	0.7714	0.1058
TINQ	0.9386	0.9417	0.7940	0.0827

Table 7. Validity on memory thresholds in visual memory capacity block. The best performance is highlighted.

Memory Thresholds	SRCC↑	PLCC↑	KRCC↑	RMSE↓
1	0.9307	0.9353	0.7722	0.0954
5	0.9248	0.9316	0.7695	0.1037
10	0.9116	0.9182	0.7495	0.1021
15	0.8949	0.9054	0.7274	0.1038
Adaptive 1 to 5	0.9386	0.9417	0.7940	0.0827
Adaptive 1 to 10	0.9328	0.9364	0.7817	0.0832

temporal inconsistency videos in both spatial and temporal modules. **Coarse Spatial Branch** refers to only using the coarse scene spatial extractor. **Fine Spatial Branch** refers to only using the fine scene spatial extractor. The model’s performance drops significantly without the DW-SA Transformer blocks, inconsistency guidance, or memory capacity, highlighting their critical role in accuracy. The coarse spatial branch alone shows a marked decline, emphasizing the need to combine both coarse and fine features. Overall, the full TINQ model outperforms its simplified variants, confirming its effectiveness in video quality prediction.

4.7. Validity on Memory Thresholds

Table 7 shows that increasing memory thresholds from 1 to 15 decreases the performance of TINQ, particularly in SRCC, from 0.9307 to 0.8949. However, using adaptive memory thresholds improves its performance, especially the adaptive 1 to 5 configuration. This suggests that dynamic memory allocation enhances the model’s accuracy in video quality prediction, which aligns better with the human visual system.

5. Conclusion

This paper presents TINQ, a novel metric for blind video quality assessment that leverages temporal inconsistency

for improved evaluation. In the SR scenario, the amplified temporal inconsistency should exclude the reference motion affection, while in the UGC scenario, although reference is unavailable, the temporal inconsistency information is proven to be effectively explored in motion information. TINQ underscores the importance of temporal inconsistency in achieving accurate video quality predictions. The framework first integrates a spatial module that extracts coarse and fine inconsistency features, in which a novel DW-SA Transformer is proposed. It then introduces a two-stage, inconsistency-guided temporal module with a visual memory capacity block to dynamically allocate memory threshold during temporal aggregation. Additionally, the Consistency-aware Fusion Unit enables temporal aggregation across different time scales. Experimental results on both SR and UGC video quality datasets confirm TINQ’s superior performance in blind video quality assessment, demonstrating its robust generalization across diverse distortion scenarios.

A. More Details for the Method

A.1. More Details of Spatial Module

The details of the spatial module in the proposed TINQ method are illustrated in Figure S5. The coarse scene spatial extractor is the proposed Deformable Window Super Attention (DW-SA) Transformer, which replaces the third stage of the Swin Transformer with the DW-SA blocks. There are two main reasons for not replacing all the Swin Transformer blocks with DW-SA blocks:

1) Studies [8,52] have shown that deformable techniques are more effective in the later layers of a network, as applying them in the early stages may lead to optimization or convergence issues;

2) Deformable techniques introduce additional parameters, as shown in Table S8. But the performance gain is significant. Since the majority of Swin-T [23]’s main blocks contribute in the third stage, the use of only DW-SA blocks in this stage helps maintain the main proportion of novel DW-SA blocks while controlling the model’s overall parameter count.

The fine scene spatial extractor is ResNet [15] pretrained on the ImageNet-1k dataset. The TINQ can reach the highest performance by combining both coarse scene spatial feature and fine scene spatial feature, as illustrated in Section C.5.

A.2. Designs of Memory Threshold

We randomly selected four videos from the VSR-QAD dataset, and their distributions of the level of temporal inconsistencies of frames are shown in Figure S6 and Figure S7, along with fitted Gaussian models. In the temporal module, we propose the following memory threshold calculation

Table S8. The testing comparison on VSR-QAD dataset of utilizing the proposed DW-SA Transformer and Swin Transformer (Swin-T).

Model	SRCC↑	PLCC↑	KRCC↑	RMSE↓	Params/M
Swin-T	0.8908	0.9088	0.7158	0.1164	26.29
DW-SA-T	0.9372	0.9395	0.7958	0.0915	26.66

method:

$$\begin{aligned}
 C_I^{ij} &= \alpha \times (\sigma(M(V_I^{ij}))) + (1 - \alpha) \times (\sigma(D(V_I^{ij}))), \\
 C_I^i &= \mu(\{C_I^{ij} \mid j = 1, \dots, F\}) \\
 &\quad + \sigma(\{C_I^{ij} \mid j = 1, \dots, F\}), \\
 T_D^i &= 5 - 4 \times \frac{C_I^i - \text{MIN}(\{C_I^i\})}{\text{MAX}(\{C_I^i\}) - \text{MIN}(\{C_I^i\})}, \\
 i &= 1, \dots, N; j = 1, \dots, F.
 \end{aligned} \tag{17}$$

where N, F are the number of videos and frame count for each video, respectively. $M(\cdot)$ refers to magnitude computation, and $D(\cdot)$ calculates the direction of the difference between adjacent frames, generating a histogram of the direction, and then the standard deviation of the histogram represents the directional consistency. μ, σ refer to mean and standard deviation calculation, respectively. α is a hyperparameter, which is detailed in Section C.2. C_I^{ij}, C_I^i are the levels of temporal inconsistency for each frame and the whole inconsistency video V_I^i , respectively. T_D^i is the memory threshold of the i -th distorted video. The rationality analysis is as follows:

1) Since the level of temporal inconsistency $\{C_I^{ij}\}$ of different videos can be well fitted by Gaussian distributions, therefore, $\mu(\cdot) + \sigma(\cdot)$ can represent the overall level of temporal inconsistency C_I^i .

2) The mean and variance of $\{C_I^{ij}\}$ vary across videos with different levels of distortion, thus making the memory threshold dynamically allocated.

B. More Details for the Dataset

Table S9 presents the key characteristics of three video quality assessment datasets: KoNViD-1K [17], LIVE-VQC [33], and VSR-QAD [48]. KoNViD-1K consists of 1,200 videos with 8-second durations, 540p resolution, and frame rates between 24 and 25 fps, focused on natural distortions. LIVE-VQC includes 585 videos, each 10 seconds long, with varying resolutions (240p to 1080p) and a frame rate of 30 fps, also targeting natural distortions. VSR-QAD contains 2,260 videos from 113 scenes, each 6 seconds in length, with 1080p resolution and a frame rate ranging from 24 to 60 fps, specifically addressing super-resolution distortions.

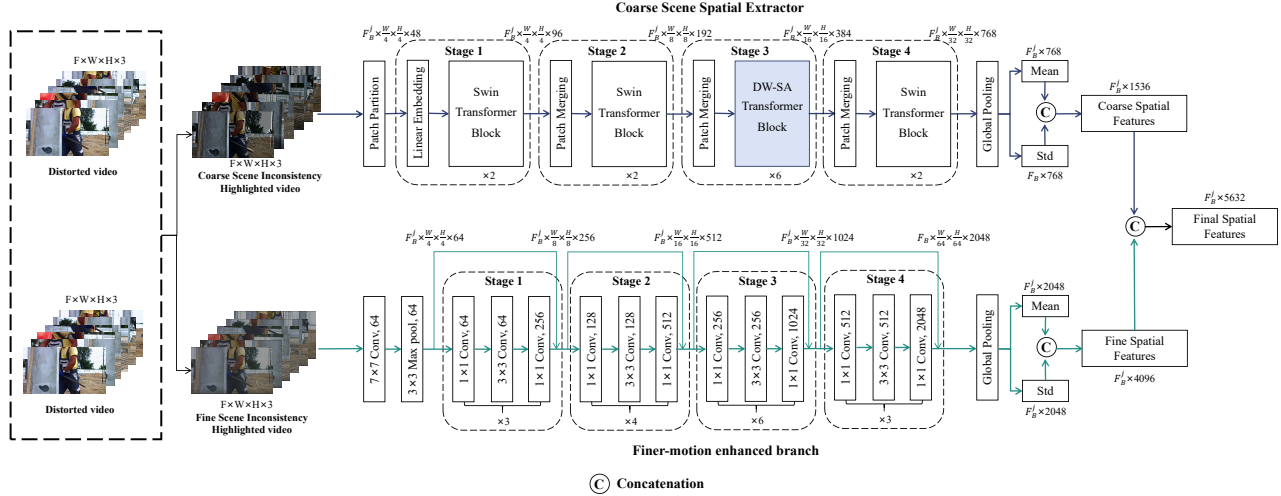


Figure S5. The **Inconsistency Highlighted Spatial Module** in the proposed **TINQ** includes detailed frameworks for both the Coarse Scene Spatial Extractor and the Fine Scene Spatial Extractor. Each layer of these extractors, along with the input and output feature dimensions, is described. The input frame batch for the j -th iteration is denoted as F_B^j , where B represents the batch size, and W and H correspond to the frame’s width and height, respectively. It is important to note that the Fine Scene Spatial Extractor processes input frames in their original resolution, while the Coarse Scene Spatial Extractor resizes the input frames to 224×224 for feature extraction.

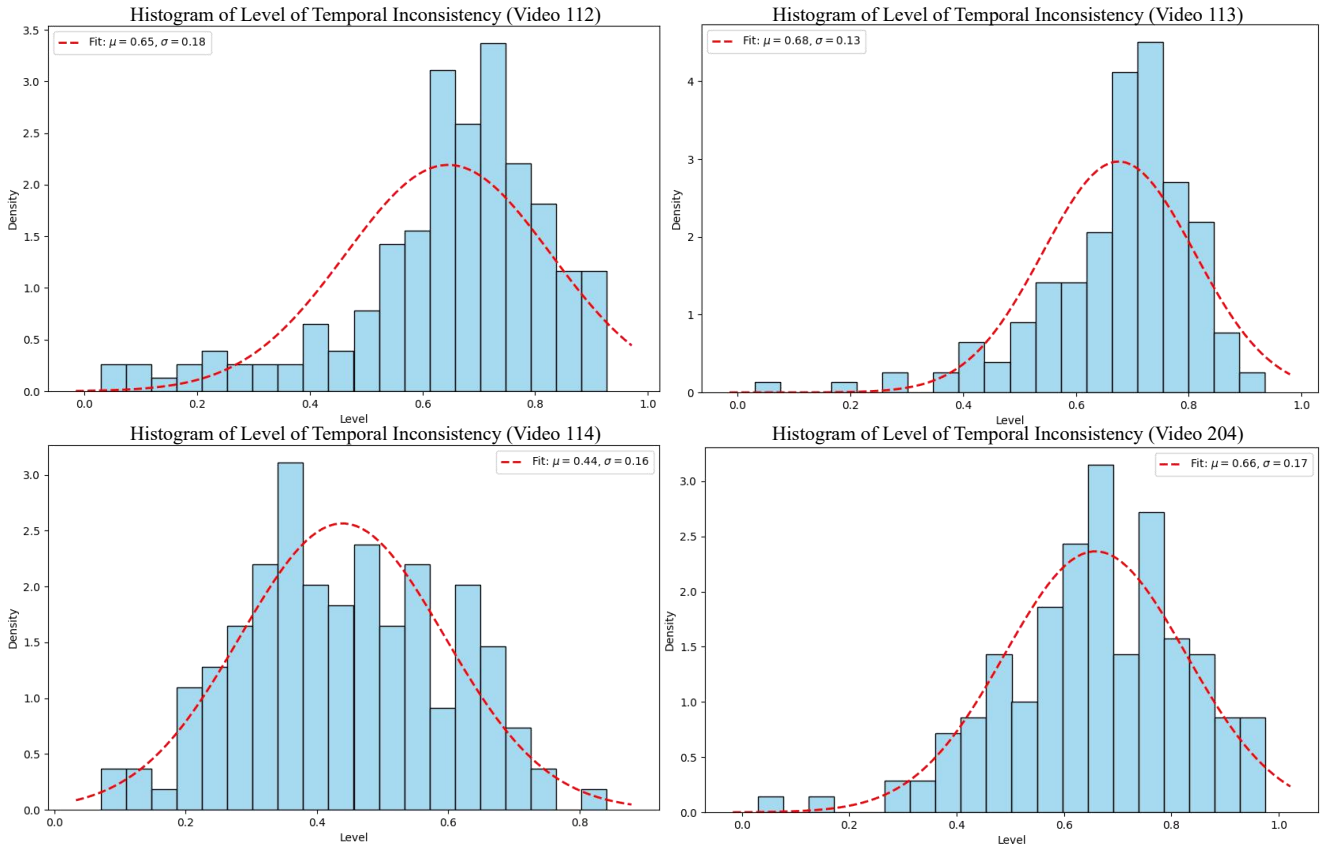


Figure S6. Examples of the histograms of the distribution of temporal inconsistency level in all frames of four videos. It can be observed that the distributions can be fitted as the Gaussian distribution.

C. More Results

In this section, ablation studies on hyper-parameters, loss functions, model parameters, and further ablation on UGC

datasets are displayed, which fully demonstrate the effec-

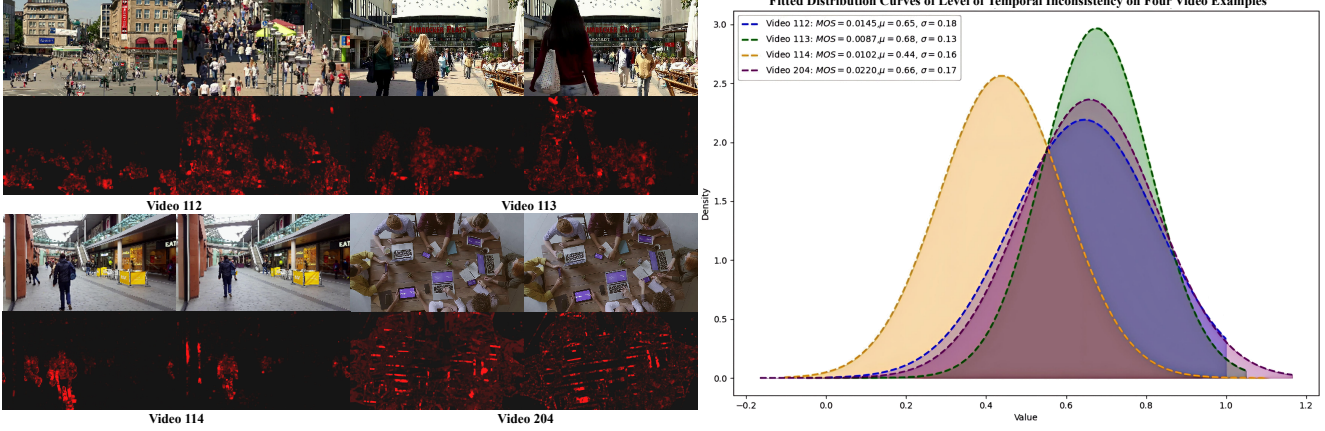


Figure S7. Four examples about the distributions of level of temporal inconsistency and sampled frames. It can be observed that videos have different levels of temporal inconsistency, thus we design an adaptively allocated memory threshold in Eq. 17

Table S9. Details of video super-resolution quality assessment dataset VSR-QAD, and user-generated content video datasets KoNViD-1K, LIVE-VQC.

Dataset	Videos	Scenes	Duration (Sec)	Spatial Resolution	Frame Rate	Distortion Category
KoNViD-1K [17]	1,200	1,200	8	540p	24,25,30	Natural
LIVE-VQC [33]	585	585	10	240p-1080p	30	Natural
VSR-QAD [48]	2,260	113	6	1080p	24-60	Super-Resolution

tiveness and robustness of the proposed method.

C.1. Validity of Loss Function

In our experiments, we attempted to use both L1 loss and MSE loss, and added SRCC as a penalty term based on these two losses. The calculation is as follows:

$$\begin{aligned} \mathcal{L}_{L_1 \& SRCC} &= \mathcal{L}_{L_1} + (1 - SRCC) \\ \mathcal{L}_{MSE \& SRCC} &= \mathcal{L}_{MSE} + (1 - SRCC). \end{aligned} \quad (18)$$

The experimental results are shown in Table S10, where each loss was evaluated by three random splits of the dataset (these three repeated tests differ from the ten repetitions mentioned in the main text, leading to slight differences in the average results). It can be observed that the MSE & SRCC loss achieved the best performance, while the difference between the effects of L1 loss and MSE loss was minimal.

Table S10. Validity of different loss functions.

Loss	SRCC \uparrow	PLCC \uparrow	KRCC \uparrow	RMSE \downarrow
L1 Loss	0.9261	0.9294	0.7680	0.0998
L1&SRCC Loss	0.9410	0.9424	0.7936	0.0869
MSE Loss	0.9294	0.9331	0.7713	0.0919
MSE&SRCC Loss	0.9437	0.9446	0.7979	0.0816

We further performed a T-test on the SRCC results of different loss functions, with the outcomes shown in the

Table S11. The P-values between L_1 and $L_1 \& SRCC$ is 0.01919, L_1 and MSE is 0.12025, L_1 and $MSE \& SRCC$ is 0.00368, L_1 and $SRCC \& MSE$ is 0.03986, $L_1 \& SRCC$ and $MSE \& SRCC$ is 0.58564, MSE and $MSE \& SRCC$ is 0.00687.

Table S11. Results of the two sample T-test performance between SRCC values obtained by different loss functions.

Loss	L1 Loss	L1-SRCC Loss	MSE Loss	MSE&SRCC Loss
L1 Loss	0	-1	0	-1
L1-SRCC Loss	1	0	1	0
MSE Loss	0	-1	0	-1
MSE&SRCC Loss	1	0	1	0

C.2. Validity of Hyper-parameter α

Table S12 presents an ablation on the hyper-parameter α , which controls the balance between magnitude and direction complexities when calculating level of temporal inconsistency. The model performs best at $\alpha = 0.5$, achieving the highest SRCC (0.9386), PLCC (0.9417), KRCC (0.7940), and lowest RMSE (0.0827). Performance decreases at the extremes ($\alpha = 0.1$ and $\alpha = 0.9$), indicating that a balanced approach between the two complexities is most effective.

Table S12. Ablation on the hyper-parameter α , which determines the weight of the magnitude complexity and complexity of direction consistency when computing the level of temporal inconsistency for each frame.

α	SRCC \uparrow	PLCC \uparrow	KRCC \uparrow	RMSE \downarrow
0.1	0.9314	0.9353	0.7823	0.1009
0.3	0.9327	0.9411	0.7787	0.0998
0.5	0.9386	0.9417	0.7940	0.0827
0.7	0.9299	0.9353	0.7835	0.0867
0.9	0.9289	0.9364	0.7819	0.1030

C.3. Validity of Hyper-parameter – γ

The hyper-parameter gamma is used to weight the prediction quality scores S_1 and S_2 of two stages. As shown in Table S13, as γ gradually increases from 0 to 1, the performance first increases and then decreases, with the best performance in the range of [0.4, 0.6].

Table S13. Ablation on the hyper-parameter γ , which determines the proportion of predicted scores S_1 and S_2 at multi time scales in the final predicted score S .

γ	SRCC \uparrow	PLCC \uparrow	KRCC \uparrow	RMSE \downarrow
0.0	0.9189	0.9308	0.7641	0.1055
0.2	0.9263	0.9353	0.7727	0.0939
0.4	0.9317	0.9375	0.7834	0.0908
0.5	0.9386	0.9417	0.7940	0.0827
0.6	0.9279	0.9361	0.7792	0.0904
0.8	0.9184	0.9274	0.7636	0.0898
1.0	0.9098	0.9197	0.7481	0.0915

Table S14. Comparisons of performance and number of parameters of 11 state-of-the-art methods. Note that the number of parameters of methods that contain several modules is the sum of each module.

Model	SRCC \uparrow	PLCC \uparrow	KRCC \uparrow	RMSE \downarrow	Paras/M
DISQ [44]	0.6421	0.6498	0.4653	0.2024	76.18
DR-IQA [45]	0.7074	0.7163	0.5369	0.1843	13.39
STF [47]	0.7629	0.7691	0.5942	0.1629	11.34
VSR-QAD [48]	0.8601	0.8681	0.6872	0.1253	23.74
DeepSRQ [49]	0.6665	0.6556	0.4741	0.1949	4.36
VSFA [22]	0.8081	0.8123	0.6301	0.1524	24.05
GSTVQA [5]	0.8278	0.8251	0.6453	0.1473	16.06
STI-VQA [51]	0.8228	0.8293	0.6479	0.1469	89.37
2Bi-VQA [36]	0.7766	0.8099	0.5854	0.6649	25.58
MBVQA [39]	0.8924	0.9008	0.7167	0.1057	127.55
TINQ	0.9372	0.9395	0.7958	0.0915	50.53

C.4. Model Parameters Analysis

Table S14 compares 11 state-of-the-art video quality assessment (VQA) methods in terms of performance and parameter count. Performance metrics include SRCC, PLCC, KRCC, and RMSE, while the parameter count is shown in

Mbyte (M). TINQ achieves the best overall performance with the highest SRCC (0.9372), PLCC (0.9395), and KRCC (0.7958), along with the lowest RMSE (0.0915). Despite having fewer parameters (50.53M), TINQ outperforms other models such as MBVQA, which has the highest parameter count (127.55M) but lower performance. Models like DeepSRQ and STF have fewer parameters but also demonstrate relatively lower performance.

C.5. Ablation Study on UGC Datasets

Table S15. The ablation study on two UGC datasets: KoNViD-1K and LIVE-VQC. “w/o” indicates “without”. “Fine” and “Coarse” represent the use of spatial features extracted solely by the Fine Scene Spatial Extractor and the Coarse Scene Spatial Extractor, respectively.

Model	Dataset		KoNViD-1K		LIVE-VQC	
	Fine	Coarse	SRCC \uparrow	PLCC \uparrow	SRCC \uparrow	PLCC \uparrow
w/o	✓	×	0.772	0.787	0.769	0.818
Inconsistency Guidance	×	✓	0.623	0.664	0.658	0.771
with	✓	×	0.804	0.816	0.770	0.832
Inconsistency Guidance	×	✓	0.780	0.818	0.807	0.810
with	✓	✓	0.709	0.720	0.671	0.808
Inconsistency Guidance	✓	✓	0.842	0.844	0.808	0.838

Table S15 highlights the significant improvement brought by incorporating inconsistency guidance in video quality assessment models when applied to UGC datasets, KoNViD-1K and LIVE-VQC. Models without inconsistency guidance show relatively weaker performance, especially when relying only on coarse-grained features, which limits their ability to predict video quality accurately. On the other hand, incorporating inconsistency guidance leads to substantial improvements in SRCC and PLCC scores across datasets, particularly when combining fine-grained and coarse-grained features. For instance, the SRCC on KoNViD-1K rises from 0.804 to 0.842, demonstrating the critical role of temporal inconsistency in enhancing prediction accuracy.

C.6. Visualization

We visualized the optical flows of the SR videos and their corresponding reference videos, and derived temporal inconsistency information through their difference. Compared to techniques like optical flow that measure traditional motion information, temporal inconsistency videos provide a clearer representation of temporal inconsistencies in SR distortions. Additionally, when comparing our prediction results with quality predictions from two state-of-the-art BVQA methods, we found our method’s predictions closest to Mean Opinion Scores (MOS).

References

- [1] Christos G. Bampis, Praful Gupta, Rajiv Soundararajan, and Alan C. Bovik. SpEED-QA: Spatial efficient entropic differ-

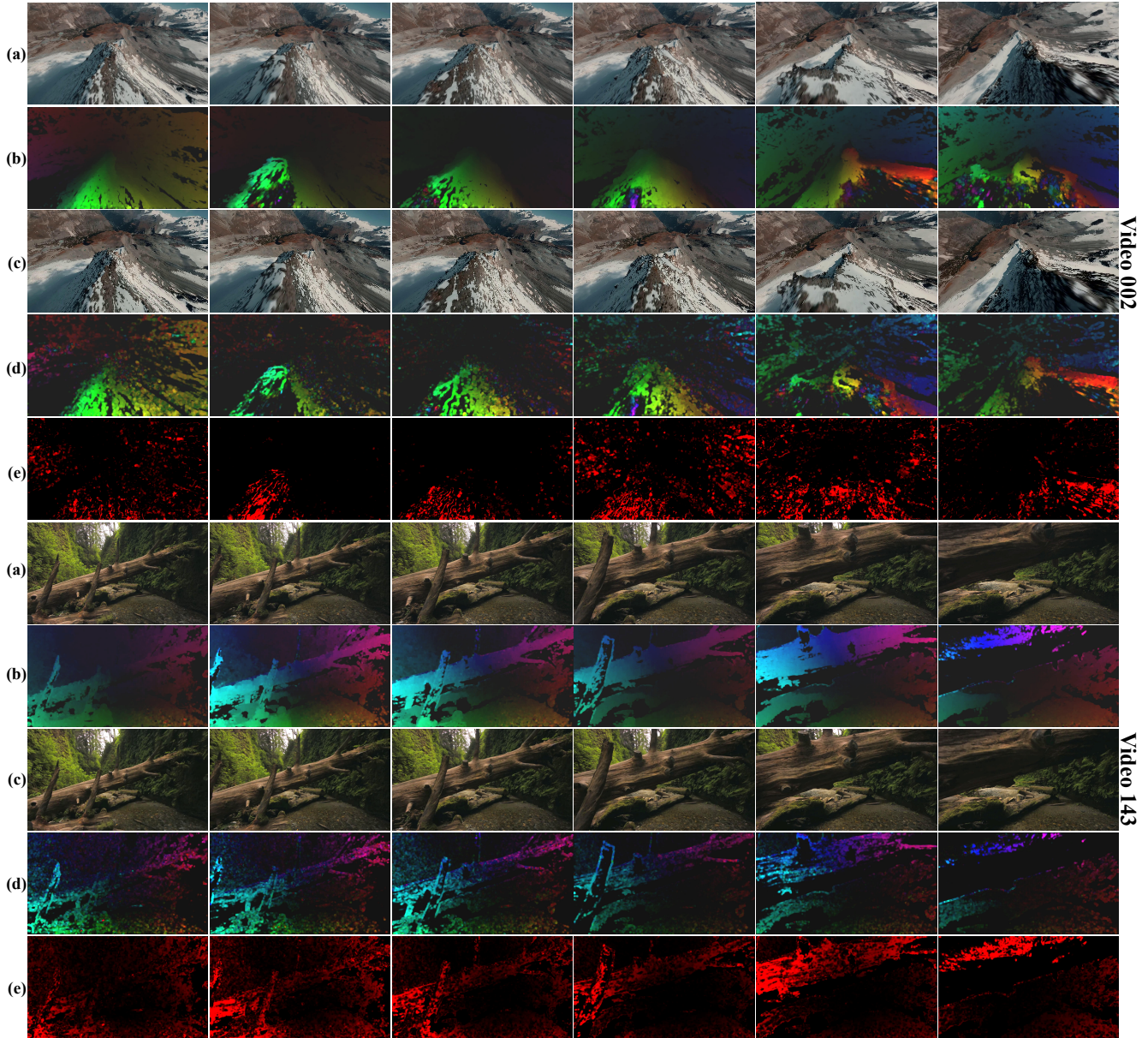


Figure S8. Visualization (Part I) presents examples of three distorted videos of VSR-QAD dataset along with their corresponding reference videos, optical flows, and temporal inconsistency videos. The rows from (a) to (e) denote the reference video, optical flow of the reference video, the distorted video, optical flow of the distorted video, and the temporal inconsistency video. Columns from left to right display consecutive frames sampled from the videos, with the sampling frame gap equal to the frame rate (FPS). Since all videos in this dataset are 6 seconds, one frame is sampled per second, resulting in a total of 6 frames per video for visualization.

- encing for image and video quality. *IEEE Signal Processing Letters*, 24(9):1333–1337, 2017. 2, 3, 7
- [2] Mehdi Banitalebi-Dehkordi, Abbas Ebrahimi-Moghadam, Morteza Khademi, and Hadi Hadizadeh. No-reference video quality assessment based on visual memory modeling. *IEEE Transactions on Broadcasting*, 66(3):676–689, 2020. 2, 3
- [3] Xiaodong Bi, Xiaohai He, Shuhua Xiong, Zeming Zhao, Honggang Chen, and Raymond Edward Sheriff. Blind video quality assessment based on spatio-temporal feature resolver.

- Neurocomputing*, 574:127249, 2024. 2
- [4] Kelvin C.K. Chan, Shangchen Zhou, Xiangyu Xu, and Chen Change Loy. BasicVSR++: Improving video super-resolution with enhanced propagation and alignment. In *IEEE CVPR*, 2022. 2
- [5] Baoliang Chen, Lingyu Zhu, Guo Li, Fangbo Lu, Hongfei Fan, and Shiqi Wang. Learning generalized spatial-temporal deep feature representation for no-reference video quality assessment. *IEEE TCSVT*, 32(4):1903–1916, 2022. 2, 7, 12

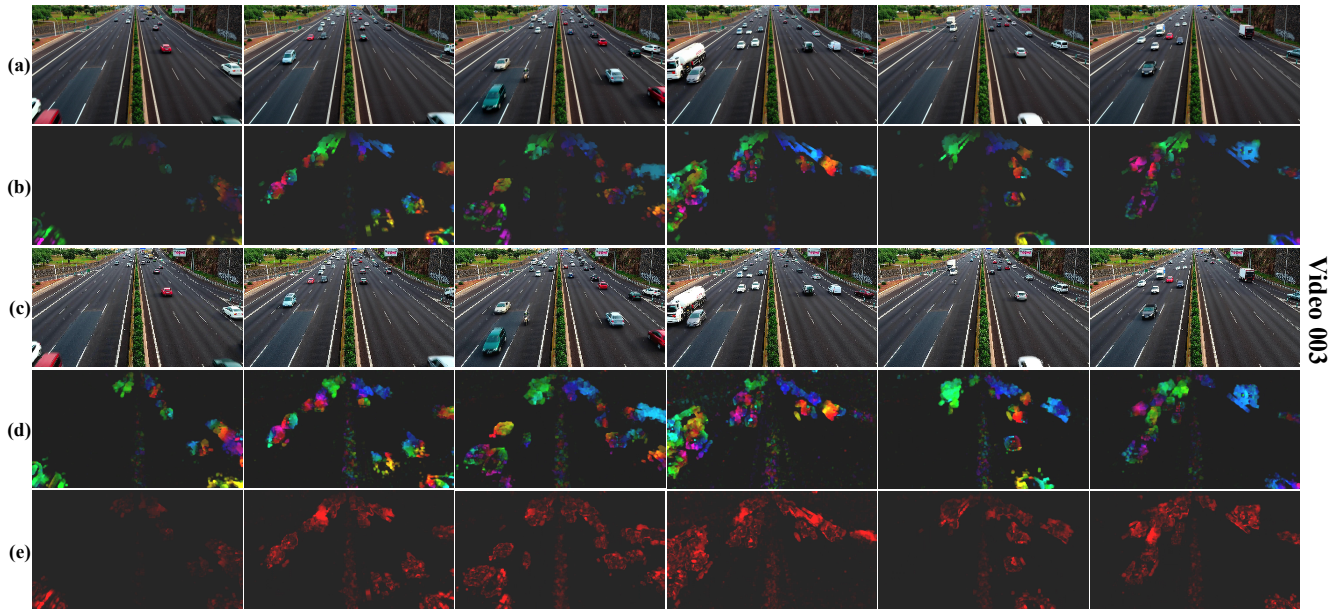


Figure S9. Visualization (Part II). The MOS/Quality Prediction of VSFA/MBVQA/TINQ(Ours) are as follows: (Video 002) 0.79426/0.77129/0.69330/**0.79185**; (Video 143) 0.50574/0.78472/0.47750/**0.50683**; (Video 003) 0.15073/0.89866/0.45200/**0.14178**.

- [6] Junyoung Chung, Çağlar Gülçehre, Kyunghyun Cho, and Yoshua Bengio. Empirical evaluation of gated recurrent neural networks on sequence modeling. *ArXiv*, abs/1412.3555, 2014. [6](#)
- [7] Nelson Cowan. The magical number 4 in short-term memory: A reconsideration of mental storage capacity. *Behavioral and Brain Sciences*, 24:87 – 114, 2001. [3](#), [5](#), [6](#)
- [8] Jifeng Dai, Haozhi Qi, Yuwen Xiong, Yi Li, Guodong Zhang, Han Hu, and Yichen Wei. Deformable convolutional networks. In *IEEE ICCV*, pages 764–773, 2017. [4](#), [9](#)
- [9] Laura Dempere-Marco, David Melcher, and Gustavo Deco. Effective visual working memory capacity: An emergent effect from the neural dynamics in an attractor network. *PLoS ONE*, 7, 2012. [3](#), [5](#), [6](#)
- [10] Jia Deng, Wei Dong, Richard Socher, Li-Jia Li, Kai Li, and Li Fei-Fei. ImageNet: A large-scale hierarchical image database. In *IEEE CVPR*, pages 248–255, 2009. [5](#)
- [11] Blaire Dube and Naseem Al-Aidroos. Distinct prioritization of visual working memory representations for search and for recall. *Attention, Perception, & Psychophysics*, 81:1253 – 1261, 2019. [3](#), [5](#), [6](#)
- [12] Joshua Peter Ebenezer, Zaixi Shang, Yongjun Wu, Hai Wei, Sriram Sethuraman, and Alan C. Bovik. ChipQA: No-reference video quality prediction via space-time chips. *IEEE TIP*, page 8059–8074, 2020. [2](#), [3](#)
- [13] Rafael Gonzalez, Richard Woods, and Barry Masters. Digital image processing, third edition. *Journal of Biomedical Optics*, 14:029901, 2009. [4](#)
- [14] Jasper E. Hajonides, Freek van Ede, Mark G. Stokes, and Anna Christina Nobre. Comparing the prioritization of items and feature-dimensions in visual working memory. *Journal of Vision*, 20, 2020. [3](#), [5](#), [6](#)
- [15] Kaiming He, Xiangyu Zhang, Shaoqing Ren, and Jian Sun. Deep residual learning for image recognition. In *IEEE CVPR*, pages 770–778, 2016. [2](#), [5](#), [9](#)
- [16] Sepp Hochreiter and Jürgen Schmidhuber. Long short-term memory. *Neural Computation*, 9(8):1735–1780, 1997. [6](#)
- [17] Vlad Hosu, Franz Hahn, Mohsen Jenadeleh, Hanhe Lin, Hui Men, Tamás Szirányi, Shujun Li, and Dietmar Saupe. The konstanz natural video database (KoNViD-1k). In *IEEE International Conference on Quality of Multimedia Experience*, pages 1–6, 2017. [1](#), [2](#), [3](#), [7](#), [9](#), [11](#)
- [18] Hassan Imani, Md Baharul Islam, and Lai-Kuan Wong. A new dataset and transformer for stereoscopic video super-resolution. *IEEE CVPRW*, pages 705–714, 2022. [2](#)
- [19] Jari Korhonen. Two-level approach for no-reference consumer video quality assessment. *IEEE TIP*, 28(12):5923–5938, 2019. [2](#), [3](#), [7](#)
- [20] Dawa Chyophel Lepcha, Bhawna Goyal, Ayush Dogra, and Vishal Goyal. Image super-resolution: A comprehensive review, recent trends, challenges and applications. *Information Fusion*, 91:230–260, 2023. [2](#)
- [21] Bowen Li, Weixia Zhang, Meng Tian, Guangtao Zhai, and Xianpei Wang. Blindly assess quality of in-the-wild videos via quality-aware pre-training and motion perception. *IEEE TCSVT*, 32(9):5944–5958, 2022. [2](#), [3](#)
- [22] Dingquan Li, Tingting Jiang, and Ming Jiang. Quality assessment of in-the-wild videos. In *ACM International Conference on Multimedia*, page 2351–2359, 2019. [2](#), [3](#), [7](#), [12](#)
- [23] Ze Liu, Yutong Lin, Yue Cao, Han Hu, Yixuan Wei, Zheng Zhang, Stephen Lin, and Baining Guo. Swin Transformer: Hierarchical vision transformer using shifted windows. In *ICCV*, 2021. [2](#), [4](#), [5](#), [9](#)
- [24] Shankhanil Mitra and Rajiv Soundararajan. Multiview contrastive learning for completely blind video quality assess-

- ment of user generated content. In *ACM International Conference on Multimedia*, page 1914–1924. Association for Computing Machinery, 2022. 7
- [25] Marta Orduna, César Díaz, Lara Muñoz, Pablo Pérez, Ignacio Benito, and Narciso García. Video multimethod assessment fusion (VMAF) on 360VR contents. *IEEE Transactions on Consumer Electronics*, 66(1):22–31, 2020. 7
- [26] Bradley R. Postle. The cognitive neuroscience of visual short-term memory. *Current Opinion in Behavioral Sciences*, 1:40–46, 2015. 3
- [27] Michele A. Saad, Alan C. Bovik, and Christophe Charrier. Blind prediction of natural video quality. *IEEE TIP*, page 1352–1365, 2014. 2, 3
- [28] Valerio Santangelo and Emiliano Macaluso. Visual salience improves spatial working memory via enhanced parieto-temporal functional connectivity. *The Journal of Neuroscience*, 33:4110–4117, 2013. 3
- [29] Maike Schmidt, Suk-Won Jin, Alane M. Gray, Dimitris Beis, Thinh Pham, Gretchen D. Frantz, Susan Palmieri, Kenneth San Francisco Hillan, Didier Y. R. Stainier, Frederic J. de Sauvage, and Weilan Ye. Capacity limit of visual short-term memory in human posterior parietal cortex. *Nature*, 428:751–754, 2004. 3, 5, 6
- [30] H.R. Sheikh and A.C. Bovik. Image information and visual quality. *IEEE TIP*, 15(2):430–444, 2006. 7
- [31] Wenzhe Shi, Jose Caballero, Ferenc Huszár, Johannes Totz, Andrew P. Aitken, Rob Bishop, Daniel Rueckert, and Zehan Wang. Real-time single image and video super-resolution using an efficient sub-pixel convolutional neural network. In *IEEE CVPR*, pages 1874–1883, 2016. 4
- [32] Natasha Sigala, Zsuzsa Kaldy, and Greg D Reynolds. Editorial: The cognitive neuroscience of visual working memory, volume II. *Frontiers in Systems Neuroscience*, 16, 2022. 3
- [33] Zeina Sinno and Alan Conrad Bovik. Large-scale study of perceptual video quality. *IEEE TIP*, 28(2):612–627, 2019. 2, 3, 7, 9, 11
- [34] Wei Sun, Xionguo Min, Wei Lu, and Guangtao Zhai. A deep learning based no-reference quality assessment model for UGC videos. In *ACM International Conference on Multimedia*, page 856–865, 2022. 2, 7
- [35] Lijuan Tang, Kezheng Sun, Luping Liu, Guangcheng Wang, and Yutao Liu. A reduced-reference quality assessment metric for super-resolution reconstructed images with information gain and texture similarity. *Signal Processing: Image Communication*, 79:32–39, 2019. 7
- [36] Ahmed Telili, Sid Ahmed Fezza, Wassim Hamidouche, and Hanene F. Z. Brachemi Meftah. 2BiVQA: Double bi-lstm-based video quality assessment of ugc videos. *ACM Trans. Multimedia Comput. Commun. Appl.*, 20(4), 2023. 2, 7, 12
- [37] Zhengzhong Tu, Chia-Ju Chen, Yilin Wang, Neil Birkbeck, Balu Adsumilli, and Alan C. Bovik. Video quality assessment of user generated content: A benchmark study and a new model. In *IEEE International Conference on Image Processing*, 2021. 2, 7
- [38] Zhou Wang, A.C. Bovik, H.R. Sheikh, and E.P. Simoncelli. Image quality assessment: from error visibility to structural similarity. *IEEE TIP*, 13(4):600–612, 2004. 7
- [39] Wen Wen, Mu Li, Yabin Zhang, Yiting Liao, Junlin Li, Li Zhang, and Kede Ma. Modular blind video quality assessment. In *IEEE CVPR*, pages 2763–2772, 2024. 2, 3, 7, 12
- [40] Jiahua Xu, Jing Li, Xingguang Zhou, Wei Zhou, Baichao Wang, and Zhibo Chen. Perceptual quality assessment of internet videos. In *Proceedings of the 29th ACM International Conference on Multimedia*, pages 1248–1257, 2021. 2
- [41] Zhenqiang Ying, Maniratnam Mandal, Deepti Ghadiyaram, and Alan Bovik. Patch-VQ: ‘Patching Up’ the video quality problem. In *IEEE CVPR*, pages 14014–14024, 2021. 7, 8
- [42] Junyong You and Yuan Lin. Efficient transformer with locally shared attention for video quality assessment. In *IEEE International Conference on Image Processing*, pages 356–360, 2022. 2
- [43] Weiwei Zhang and Steven J. Luck. Discrete fixed-resolution representations in visual working memory. *Nature*, 453:233–235, 2008. 3, 5, 6
- [44] Tiesong Zhao, Yuting Lin, Yiwen Xu, Weiling Chen, and Zhou Wang. Learning-based quality assessment for image super-resolution. *IEEE TMM*, 24:3570–3581, 2022. 7, 12
- [45] Heliang Zheng, Huan Yang, Jianlong Fu, Zheng-Jun Zha, and Jiebo Luo. Learning conditional knowledge distillation for degraded-reference image quality assessment. In *IEEE ICCV*, pages 10242–10251, 2021. 7, 12
- [46] Qi Zheng, Zhengzhong Tu, Xiaoyang Zeng, Alan C. Bovik, and Yibo Fan. A completely blind video quality evaluator. *IEEE Signal Processing Letters*, 29:2228–2232, 2022. 7
- [47] Fei Zhou, Wei Sheng, Zitao Lu, Bo Kang, Mianyi Chen, and Guoping Qiu. Super-resolution image visual quality assessment based on structure–texture features. *Signal Processing: Image Communication*, 117:117025, 2023. 7, 12
- [48] Fei Zhou, Wei Sheng, Zitao Lu, and Guoping Qiu. A database and model for the visual quality assessment of super-resolution videos. *IEEE Transactions on Broadcasting*, 70(2):516–532, 2024. 1, 2, 3, 7, 9, 11, 12
- [49] Wei Zhou, Qiuping Jiang, Yuwang Wang, Zhibo Chen, and Weiping Li. Blind quality assessment for image super-resolution using deep two-stream convolutional networks. *Information Sciences*, 528:205–218, 2020. 7, 12
- [50] Wei Zhou and Zhou Wang. Quality assessment of image super-resolution: Balancing deterministic and statistical fidelity. In *ACM International Conference on Multimedia*, page 934–942. Association for Computing Machinery, 2022. 7
- [51] Hanwei Zhu, Baoliang Chen, Lingyu Zhu, and Shiqi Wang. Learning spatiotemporal interactions for user-generated video quality assessment. *IEEE TCSVT*, 33(3):1031–1042, 2023. 2, 3, 7, 12
- [52] Xizhou Zhu, Han Hu, Stephen Lin, and Jifeng Dai. Deformable Convnets V2: More deformable, better results. In *IEEE CVPR*, pages 9300–9308, 2019. 4, 9